ADVANCED FUNCTIONAL MATERIALS
www.afm-journal.de

Joint Multi-Frequency Beam Shaping and Steering via Space–Time-Coding Digital Metasurfaces

Giuseppe Castaldi, Lei Zhang, Massimo Moccia, Alisa Y. Hathaway, Wen Xuan Tang, Tie Jun Cui, and Vincenzo Galdi**

Digital programmable metasurfaces provide a very powerful and versatile platform for implementing spatio-temporal modulation schemes that are of great interest within the emerging framework of space–time metastructures. In particular, space–time-coding digital metasurfaces have been successfully applied to advanced wavefront-manipulations in both the spatial and spectral domains. However, conventional space–time-coding schemes do not allow the joint syntheses of the transmission/scattering angular responses at multiple frequencies, which are potentially useful in a variety of applications of practical interest. Here, a strategy is put forward to lift this limitation, thereby enabling joint multi-frequency beam shaping and steering, that is, the independent and simultaneous syntheses of prescribed scattering patterns at given harmonic frequencies. The proposed approach relies on a more sophisticated space–time coding, with suitably designed, and temporally intertwined coding sub-sequences, which effectively disentangles the joint multi-frequency syntheses. The power and versatility of the approach are illustrated via a series of representative application examples, including multi-beam, diffuse-scattering, and orbital-angular-momentum patterns. Theoretical predictions are experimentally validated by means of microwave measurements. The outcomes of this study hold promising potentials for applications to future imaging, information, and mobile-communication systems.

1. Introduction

Conventional metastructures, such as metamaterials and metasurfaces, are artificially engineered by arranging sub-wavelength metallic and/or dielectric inclusions in a host medium.[1,2] By suitably designing and tailoring the inclusions' responses along one or multiple spatial directions, advanced manipulations of the phase, amplitude, and polarization of electromagnetic wavefronts can be in principle attained. More recently, the increased availability of rapidly reconfigurable inclusions has granted access to the temporal dimension as well, and the field of space–time metastructures[3,4] is emerging as one of the most promising and fast-pacing research areas. A variety of new ideas, including time-modulated meta-atoms,[5] temporal multilayers,[6–11] space–time-periodic diffraction gratings,[12] Fresnel drag,[13] and time-dependent epsilon-near-zero media,[14] just to mention a few, have been proposed and explored, also revisiting old results in the field of electrical engineering[15–17] and taking inspiration from emerging concepts in classical and quantum physics such as "time-crystals."[18,19] Arguably, one of the most promising application scenarios for space–time metastructures involves breaking Lorentz reciprocity without the need of magnetic bias, and several candidate strategies have been explored theoretically[20–24] and experimentally.[25–29]

In a series of recent studies, we have been exploring a class of space–time metastructures based on the concept of "digital coding metasurface" originally introduced by Cui and co-workers.[30] These structures rely on a limited number of inclusion types (in the simplest case, only two), which not only simplifies significantly the design process, but also enables "programmable" architectures as well as "information-based" interpretations and visions with fascinating and still largely unexplored potentials.[31,32] Specifically, we proposed the concept of space–time-coding digital metasurfaces,[33] by leveraging these digital and programmable platforms, and introducing a dynamic diode-based switching of the element responses controlled in space and time by a field-programmable gate array (FPGA). We showed that the switching, described by a space–time-coding matrix, could be designed and optimized so as to attain simultaneous field manipulations in both the space and frequency domains, including harmonic beam steering and scattering-signature reduction/control. This idea has resonated in the research community, and has already found a variety

Prof. G. Castaldi, Dr. M. Moccia, Prof. V. Galdi
Fields & Waves Lab
Department of Engineering
University of Sannio
Benevento I-82100, Italy
E-mail: vgaldi@unisannio.it

Dr. L. Zhang, Prof. W. X. Tang, Prof. T. J. Cui
State Key Laboratory of Millimeter Waves
Southeast University
Nanjing 210096, China
E-mail: tjcui@seu.edu.cn

A. Y. Hathaway
Department of Electrical Engineering and Computer Science
Massachusetts Institute of Technology
Cambridge, MA 02142, USA

The ORCID identification number(s) for the author(s) of this article can be found under https://doi.org/10.1002/adfm.202007620.

DOI: 10.1002/adfm.202007620

 © 2020 Wiley-VCH GmbH

of applications, including programmable and reconfigurable nonreciprocity,[26] harmonic manipulations,[34,35] broadband spectral camouflaging,[36] wireless communications,[37] and analog computing.[38] Although most experimental validations to date are restricted to the microwave range, with the advent of increasingly faster switching schemes, for example, based on graphene[39,40] and vanadium dioxide,[41,42] applications to the terahertz range should be within reach.[43]

Among the most promising applications of the space–time-coding concept, it is worth mentioning the broad field of "intelligent reflecting surfaces," which is currently garnering a great deal of attention for future (6th-generation and beyond) wireless communication networks (e.g., see refs. [44–50] for a sparse sampling). In this context, the advanced wavefront-manipulation capabilities enabled by metasurfaces can be leveraged so as to remove the necessity of complex decoding, encoding, and radio-frequency processing blocks.

Of special interest in the above scenarios is the implementation of diversity strategies, for example, in terms of frequency, pattern, or polarization. However, basic space–time-coding schemes do not allow to synthesize independently and simultaneously the wavefront-manipulations at multiple frequencies, as a consequence of the inherent frequency spreading of the single-element response. Accordingly, in our previous study,[33] emphasis was placed on the basic physical principle and proof-of-concept validation, whereas multi-frequency syntheses were addressed without full control of the harmonic orders (e.g., deflection angles in the harmonic beam steering) and by means of brute-force numerical optimization. However, the general applicability of such optimization-based approach is severely limited by its significant computational complexity and highly nonlinear character (see the Supporting Information for some typical benchmarks). Here, we put forward a major extension which overcomes this limitation via a more sophisticated space–time coding, with suitably designed, and temporally intertwined coding sub-sequences. This provides a systematic and computationally viable route to the joint multi-frequency beam shaping and steering. To illustrate the potential of our approach, we demonstrate various examples of independent syntheses of prescribed scattering patterns at several selected harmonic frequencies. These include multi-beam, maximally flat, and orbital-angular-momentum (OAM) beam designs. For experimental validations, we fabricate and characterize a microwave (X-band) prototype, showing good agreement with our theoretical predictions.

Overall, our results sensibly enrich the wavefront-manipulation capabilities of space–time-coding digital metasurfaces, paving the way for advanced applications to wireless communications, imaging, and information systems.

2. Background Theory and Modeling

Referring to **Figure 1** for conceptual illustration, we consider a digitally programmable metasurface working in reflection mode. Specifically, the reflection phase of each element (yellow square patches in the schematic) can be switched (via one or more diode elements) among different quantized states, which can be represented in terms of a digital alphabet; in the simplest (binary) case, for instance, in-phase and out-of-phase responses can be associated with the 0/1 bits. The switching is dynamically controlled in space and time by an FPGA, according to a given coding. Overall, the platform is conceptually similar to those considered in our previous studies,[26,33] but the scope here is more ambitious, namely, to design the space–time coding so as to enable joint multi-frequency beam shaping and steering. As schematically illustrated in Figure 1, this entails the independent and simultaneous syntheses of desired scattering patterns (e.g., single and multiple beams, different beam shapes, and steering directions) at selected harmonic frequencies.

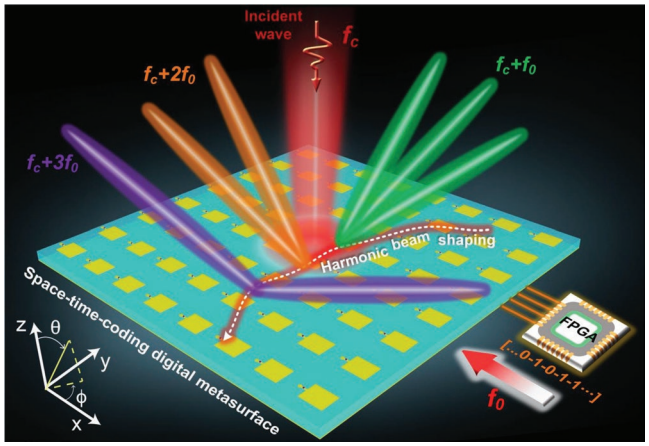

Figure 1. Conceptual illustration of the joint multi-frequency beam shaping and steering via a space–time coding-digital metasurface. Also shown is the Cartesian (and associated spherical) reference system.

From the modeling viewpoint, we assume a metasurface made of $N \times M$ identical elements arranged in the x–y plane as a periodic square lattice, with constant inter-element spacing d, under a normally incident time-harmonic illumination with suppressed $\exp(j2\pi f_c t_c)$ dependence. Moreover, we assume that the reflection coefficient of the generic (n, m) coding element is subject to a periodic modulation on a time scale much slower than the electromagnetic one, which can be ideally expressed over the period T_0 as a superposition of L rectangular pulses, viz.,

$$\Gamma^{(nm)}(t) = \sum_{l=1}^{L} \Gamma_l^{(nm)} U_l(t), \quad 0 < t < T_0 \tag{1}$$

where

$$U_l(t) = \begin{cases} 1, (l-1)T_s \le t \le lT_s \\ 0, \quad \text{otherwise} \end{cases} \tag{2}$$

represents a rectangular pulse of width $T_s = T_0/L$, and $\Gamma_l^{(nm)}$ denotes one of the possible reflection-coefficient states (at the excitation frequency f_c) of the generic (n, m) coding element. For now, we assume ideal, perfectly reflecting elements, with a number S of quantized reflection phases that span the interval (0, 360°). Thus, apart from irrelevant phase factors, for a binary ($S = 2$) configuration, we will have $\Gamma_l^{(nm)} \in \{1, -1\}$ associated with the bits {0,1}, whereas for a 2-bit configuration ($S = 4$), we

© 2020 Wiley-VCH GmbH

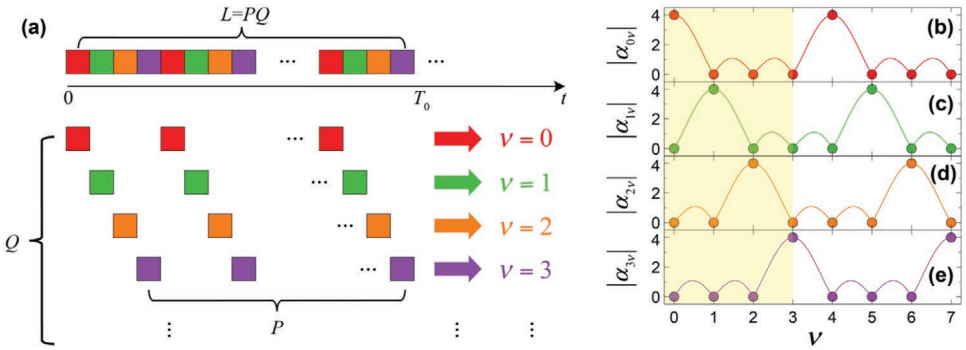

Figure 2. a) Schematic illustration of the joint multi-frequency syntheses based on intertwined sub-sequences. As indicated by the color coding, each sub-sequence affects one specific harmonic order. b–e) Responses (magnitude) of the digital-filter terms $\alpha_{q\nu}$ in Equation (9) for a 2-bit scenario ($S = 4$) and four harmonic frequencies ($P = Q = 4$), for $q = 0, 1, 2, 3$, respectively. Continuous curves are guides-to-the-eye only. Note the periodicity outside the spectral range of interest (yellow-shaded region).

will have $\Gamma_l^{(nm)} \in \{1, j, -1, -j\}$ associated with the digits {0,1,2,3}, and so on. Referring to ref. [33] for details, the time-domain scattered far-field can be approximately modeled as

$$f(\theta,\varphi,t) = E(\theta,\varphi)\sum_{n=1}^{N}\sum_{m=1}^{M}\Gamma^{(nm)}(t) \exp\left\{j\frac{2\pi d}{\lambda_c}\sin\theta\left[(n-1)\cos\varphi+(m-1)\sin\varphi\right]\right\} \tag{3}$$

where $E(\theta, \phi)$ is the far-field scattering pattern of the element, and λ_c is the wavelength (in vacuum) pertaining to the excitation frequency f_c. By expanding in Fourier series the time-modulated reflection coefficient in Equation (1), and substituting it in Equation (3), the scattered field at the harmonic frequen cy $f_c + \nu f_0$ (with $f_0 = 1/T_0$) can be written as[33]

$$F_\nu(\theta,\varphi) = E(\theta,\varphi)\sum_{n=1}^{N}\sum_{m=1}^{M}a_\nu^{(nm)} \exp\left\{j\frac{2\pi d}{\lambda_c}\sin\theta\left[(n-1)\cos\varphi+(m-1)\sin\varphi\right]\right\} \tag{4}$$

where

$$a_\nu^{(nm)} = \sum_{l=1}^{L}\frac{\Gamma_l^{(nm)}}{L}\operatorname{sinc}\left(\frac{\pi\nu}{L}\right)\exp\left[\frac{-j\pi\nu(2l-1)}{L}\right] \tag{5}$$

From Equations (4) and (5), we observe that the reflection-coefficient states $\Gamma_l^{(nm)}$ can be exploited to synthesize the equivalent complex-valued amplitudes $a_\nu^{(nm)}$ at the various harmonic frequencies. As shown in ref. [33], these equivalent amplitudes may exhibit finer and wider phase/amplitude coverage than the original quantized reflection states. However, it is also apparent from Equation (5) that the equivalent amplitudes at each harmonic order are affected by all reflection-coefficient states $\Gamma_l^{(nm)}$. This inherent entanglement significantly complicates the joint multi-frequency synthesis, as quantitatively exemplified in Figure S1, Supporting Information, for the simple case of two frequencies and 2-bit coding.

Our proposed strategy to disentangle the synthesis problem is schematically illustrated in **Figure 2**a, with reference to a generic coding element. From now on, since this procedure can be applied independently to each coding element, we will drop the superscripts (nm) for notational simplicity. Without loss of generality, the problem can be formulated as the joint syntheses at Q harmonic frequencies (including the center frequency f_c), that is, for orders $\nu = 0, 1, \ldots, Q-1$. To this aim, we decompose the coding sequence into a series of Q intertwined sub-sequences of length P, so that the total length of one period is $L = PQ$. For the sub-sequence elements, we enforce the following constrains

$$\Gamma_{q+1+pQ} = \Omega_{pq}\Gamma_{q+1}, \quad p = 0,\ldots,P-1, \quad q = 0,\ldots,Q-1 \tag{6}$$

where Ω_{pq} represent phase-shift factors belonging to the same quantized set as the reflection-coefficient states, so that the results of the products belong to that set as well; note that, for self-consistency, $\Omega_{0q} = 1$, $q = 0, \ldots, Q-1$. Accordingly, the equivalent amplitudes in Equation (5) can be recast as

$$a_\nu = c_\nu\sum_{q=0}^{Q-1}\Gamma_{q+1}\alpha_{q\nu}\exp\left(-\frac{j2\pi\nu q}{L}\right) \tag{7}$$

where

$$c_\nu = \frac{1}{L}\operatorname{sinc}\left(\frac{\pi\nu}{L}\right)\exp\left(-\frac{j\pi\nu}{L}\right) \tag{8}$$

governs the spectral decay, whereas the terms

$$\alpha_{q\nu} = \sum_{p=0}^{P-1}\Omega_{pq}\exp\left(-\frac{j2\pi\nu p}{P}\right) \tag{9}$$

can be interpreted as digital filters that can be designed via judicious choice of the phase-shift factors Ω_{pq}, so as to disentangle the syntheses. Ideally, this would require

$$\alpha_{q\nu} \propto \tilde{\delta}_{q\nu} \tag{10}$$

where

$$\tilde{\delta}_{q\nu} = \begin{cases} 1, & q = \nu \\ 0, & q \neq \nu \end{cases}, \quad q,\nu = 0,\ldots,Q-1 \tag{11}$$

© 2020 Wiley-VCH GmbH

denotes a reduced Kronecker delta (i.e., operating within a restricted range of indices). In this case, each of the Q sub-sequences would basically affect only one selected harmonic frequency, thereby enabling independent and simultaneous syntheses. As detailed in the Supporting Information, this problem admits a remarkably simple solution when the number Q of harmonic frequencies of interest is not greater than the number S of quantized reflection-phase states available. In this case, one should choose $P = S$ and

$$\Omega_{pq} = \exp\left(\frac{j2\pi pq}{S}\right) \tag{12}$$

that is, quantized linear phase gradients. Figure 2b illustrates the working mechanism for a 2-bit configuration and four harmonic frequencies ($P = Q = S = 4$). As can be observed, each of the four $\alpha_{q\nu}$ terms singles out a specific harmonic frequency. We note that, in view of the finite length of the sub-sequences, the result is not a conventional Kronecker delta, but it exhibits a periodicity of Q. This is consistent with our requirements in Equations (10) and (11), but it implies that the scattering patterns synthesized at the first Q harmonics will repeat periodically at higher orders, with progressively decreasing strengths as dictated by Equation (8). Moreover, in view of the inherent symmetry, the scattering patterns will also repeat periodically for negative values of the harmonic order.

The case with $Q > S$ does not generally admit an exact closed-form solution, and can be addressed in a weak form as an optimization problem (see Supporting Information for more details).

For clearer understanding of the effects of our proposed strategy on the joint multi-frequency syntheses, Figure S2, Supporting Information, illustrates the simple case of two frequencies and 2-bit coding. By direct comparison with Figure S1, Supporting Information, we notice that it is now possible to synthesize at both frequencies an equivalent complex-value amplitude a_ν with constant magnitude and arbitrary quantized phase.

It can be easily understood that the number of harmonic orders Q that can be independently controlled is ultimately limited by the number of available states S and the switching rate f_s of the diode elements. Assuming $P = S$ (in order to attain an exact, closed-form solution), we observe from Equations (1) and (2) that the modulation period is given by $T_0 = SQT_s$ (see also the schematic in Figure 2a), corresponding to a modulation frequency $f_0 = f_s/(SQ)$, with $f_s = 1/T_s$ denoting the diode switching rate. Therefore, for a given number of available quantized states S, and a minimum frequency separation of the harmonics $f_{0\min}$ (which depends on the specific application and, ultimately, on the spectral resolution available), the maximum number of harmonic orders that can be independently controlled is $Q_{\max} = f_s/(Sf_{0\min})$. To give an idea, in our experimental study below, we consider a 2-bit coding ($S = 4$) and a switching rate $f_s = 5$MHz for the positive-intrinsic-negative (PIN) diodes; for a number of controlled harmonic orders $Q = 4$, this yields a frequency separation $f_0 = 0.3125$ MHz, which we are able to resolve. We highlight that our choice of f_s above is mainly dictated by attaining a basic proof of concept without resorting to an exceedingly complex electronics. However, PIN diodes can reach switching rates up to hundreds of MHz, and therefore there is still ample room for increase. As previously mentioned, at higher frequencies, alternative switching schemes (e.g., based on graphene) could be exploited.

3. Results and Discussion

3.1. Representative Numerical Results

Once the synthesis at multiple frequencies has been disentangled, all the available arsenal of semi-analytical design procedures for conventional digital coding metasurfaces[30,51–55] can be separately applied at each frequency, with a negligible computational cost. To illustrate the potential of our approach, in terms of power and versatility, we consider a space–time coding-digital metasurface with 16 × 16 elements and 2-bit coding ($S = 4$), and apply our proposed procedure for the joint syntheses at $Q = 4$ harmonic frequencies (i.e., $\nu = 0, 1, 2, 3$), assuming sub-sequences of length $P = 4$; this yields a total length $L = PQ = 16$ of the time-coding sequence on a single period T_0 (see Figure 2a). As previously mentioned, the procedure is applied independently for each of the 16 × 16 coding elements. For now, we assume perfect phase responses for the coding elements, with jumps of 90°. As a general observation from our numerical simulations and previous experience, phase errors on the order of ≈±10° tend to maintain acceptable accuracy in the synthesized scattering patterns. Larger phase errors may lead to the appearance of visible undesired features (e.g., higher sidelobes) at certain harmonic orders.

As a first example, we apply the principle of scattering-pattern shift,[52] which relies on the convolution theorem to steer a given scattering pattern toward a desired direction. **Figure 3** shows the results of some representative syntheses at the four frequencies of interest. Specifically, Figure 3a–d show the synthesized phase distributions of the equivalent complex-valued amplitudes $a_\nu^{(nm)}$ at the first four harmonic frequencies (with constant magnitudes specified in the caption), whereas Figure 3e–h show the corresponding scattering patterns. In particular, at the center frequency ($\nu = 0$) we consider a stripe-type binary phase pattern (Figure 3a), which is known to generate a two-beam scattering pattern along the x-direction (Figure 3e); at the harmonic order $\nu = 1$, we combine the previous phase pattern with a linear phase gradient along the y-direction, obtaining the 2-bit pattern in Figure 3b, which steers the previous two-beam scattering pattern along the y-direction (Figure 3f). At the harmonic order $\nu = 2$, we synthesize instead a checkerboard-type binary phase pattern (Figure 3c), yielding a four-beam scattering pattern (Figure 3g). Finally, at the harmonic order $\nu = 3$ (Figure 3d,h), we implement a two-beam pattern along the y-direction, with steering along the x-direction. The complete space–time coding can be represented as a 3D matrix with 16 × 16 × 16 elements, and it is not easy to visualize; this raw data is accessible in the Supporting Information for all examples in this study.

As a second application example, we consider diffuse-scattering. For space-coding digital metasurfaces, this problem has been widely studied, and several design approaches are available.[30,51,53,54] With the same panel structure of Figure 3, **Figure 4** shows the results pertaining to four syntheses based

© 2020 Wiley-VCH GmbH

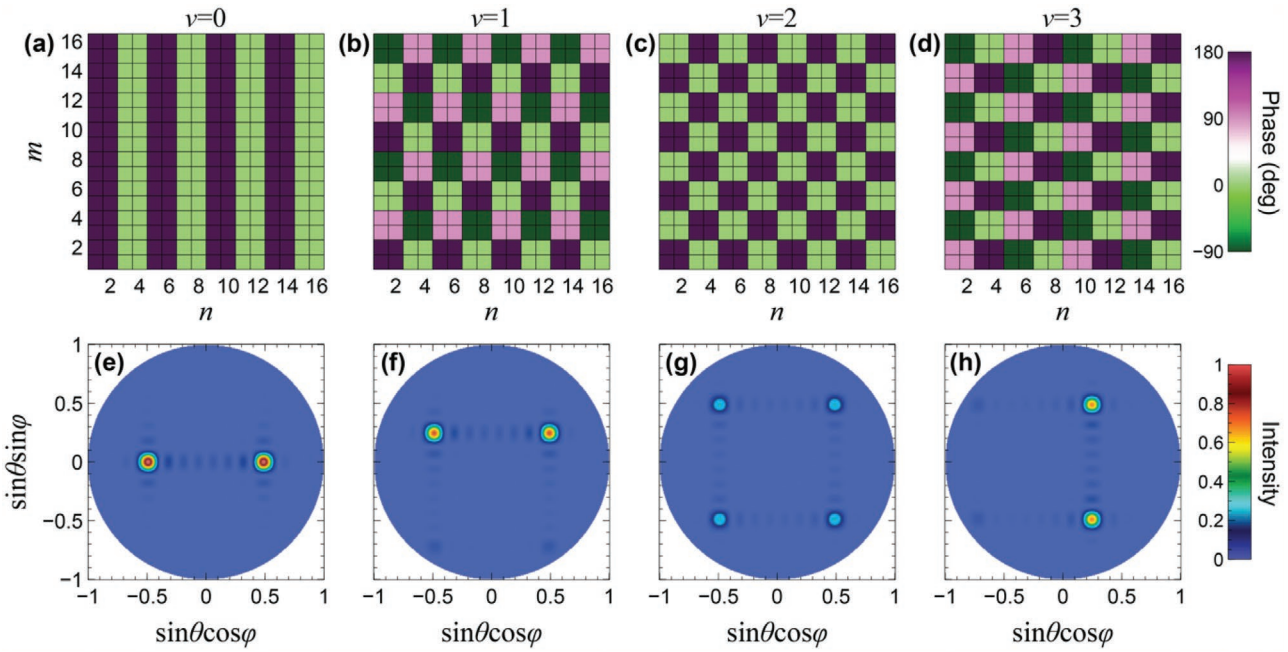

Figure 3. First numerical example of joint syntheses at $Q = 4$ frequencies, for a 16×16-element metasurface with inter-element spacing $d = \lambda_c/2$, 2-bit coding ($S = 4$), and sub-sequences of length $P = 4$. a–d) Synthesized phase patterns, in false-color scale, for the equivalent complex-valued amplitude $a_\nu^{(nm)}$ at the harmonic orders $\nu = 0, 1, 2, 3$, respectively; the corresponding (constant) magnitudes are: 0.250, 0.248, 0.244, and 0.236, respectively. e–h) Corresponding scattering patterns, in false-color scale, implementing a two-beam configuration along the x-direction, a steered version along the y-direction, a four-beam configuration, and a two-beam along the y-direction steered along the x-direction, respectively. Intensities are normalized with respect to the maximum value at the center frequency. The designed space–time-coding matrix is given in the Supporting Information.

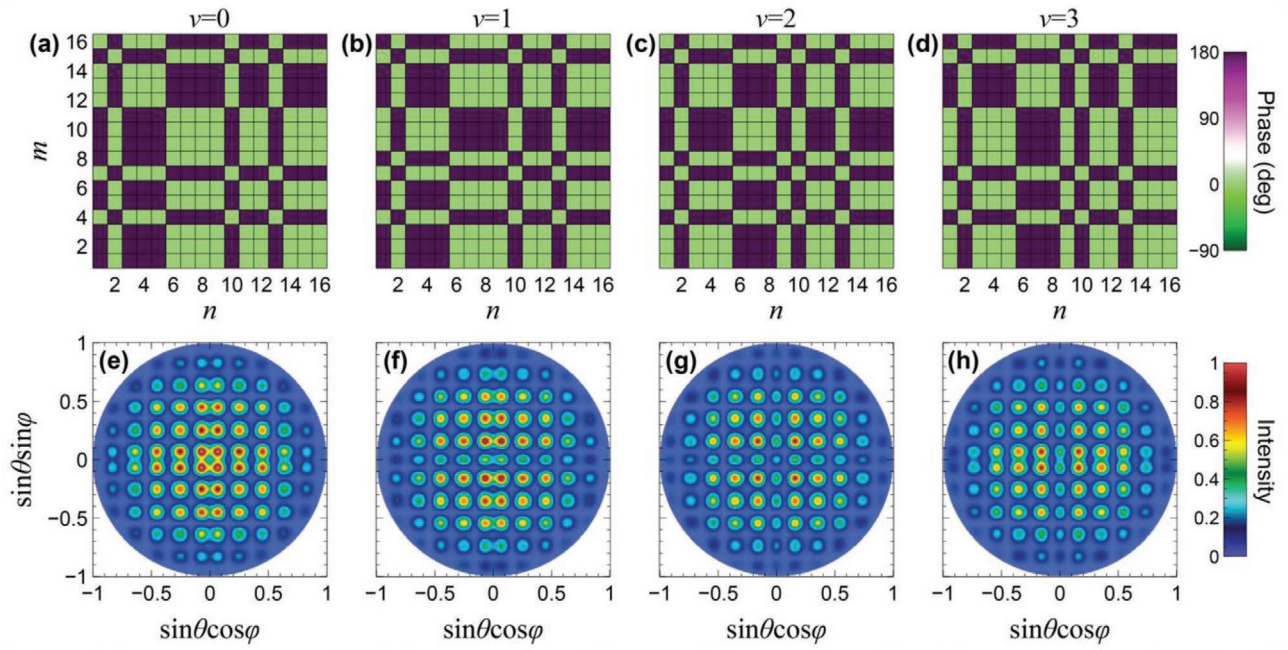

Figure 4. Second numerical example of joint syntheses at $Q = 4$ frequencies, for a 16×16-element metasurface with inter-element spacing $d = \lambda_c/2$, 2-bit coding ($S = 4$), and sub-sequences of length $P = 4$. a–d) Synthesized phase patterns, in false-color scale, for the equivalent complex-valued amplitude $a_\nu^{(nm)}$ at the harmonic orders $\nu = 0, 1, 2, 3$, respectively; the corresponding (constant) magnitudes are: 0.250, 0.248, 0.244, and 0.236, respectively. e–h) Corresponding scattering patterns, in false-color scale, implementing different combinations of GRS-type polynomials for diffuse-scattering (see Supporting Information for details). Intensities are normalized with respect to the maximum value at the center frequency. The designed space–time-coding matrix is given in the Supporting Information.

 © 2020 Wiley-VCH GmbH

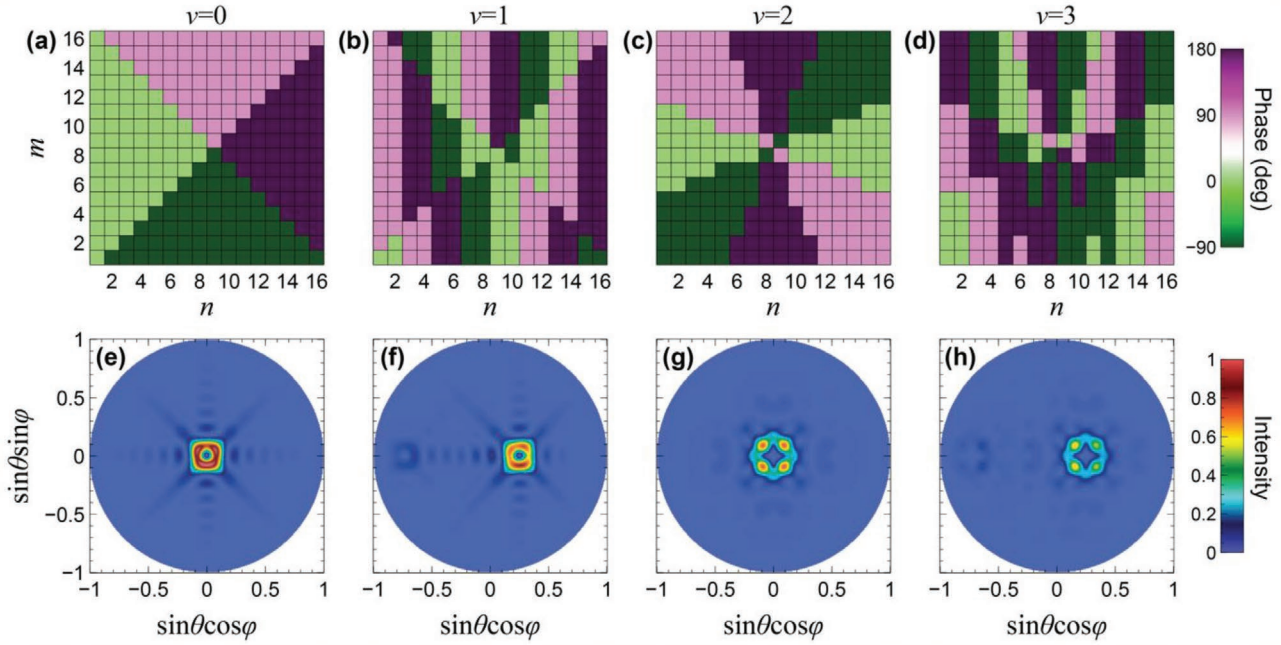

Figure 5. Third numerical example of joint syntheses at $Q = 4$ frequencies, for a 16 × 16-element metasurface with inter-element spacing $d = \lambda_c/2$, 2-bit coding ($S = 4$), and sub-sequences of length $P = 4$. a–d) Synthesized phase patterns, in false-color scale, for the equivalent complex-valued amplitude $a_\nu^{(nm)}$ at the harmonic orders $\nu = 0, 1, 2, 3$, respectively; the corresponding (constant) magnitudes are: 0.250, 0.248, 0.244, and 0.236, respectively. e–h) Corresponding scattering patterns, in false-color scale, implementing an OAM beam with topological charge l = 1, its version steered along the *x*-direction, two-beam configuration along the *x*-direction, a steered version along the *y*-direction, an OAM beam with topological charge l = 2, and its version steered along the *x*-direction, respectively. Intensities are normalized with respect to the maximum value at the center frequency. The designed space–time-coding matrix is given in the Supporting Information.

on the so-called Golay–Rudin–Shapiro (GRS) polynomials. Referring to the Supporting Information for details, these types of syntheses have been proven to be sub-optimal in terms of spectral flatness.[53,54] Interestingly, the entailed phase patterns (Figure 4a–d) are of binary type, and therefore can be implemented with simple 1-bit coding metasurfaces. Potential applications include the reduction/control of the scattering signature, based on the spreading of the scattered power uniformly in space and across the frequency spectrum. We also note that the scattering patterns (Figure 4e–h) exhibit some interesting complementary behavior among adjacent frequencies, inherited by the properties of GRS polynomials (see the Supporting Information for details). This implies that, over broad regions of the solid angle, the maxima at a harmonic frequency correspond to the minima at adjacent frequencies. This may find potentially interesting applications in communication systems, as a strategy to attain multiple frequency channels with broad, uniform spatial coverage and yet minimal interference between close-by frequencies.

As a final numerical example, we consider the synthesis of OAM beams. These types of beams have attracted a great deal of interest as a means to potentially enlarge the channel capacity in optical[56] and radio-frequency[57] links and, in spite of some inherent limitations in far-field scenarios,[58] they constitute a very active research area. **Figure 5** shows some examples of multi-frequency syntheses involving OAM beams of topological charge $\ell = 1$ (Figure 5a,e) and $\ell = 2$ (Figure 5c,g), at the center frequency and $\nu = 2$ harmonic order, respectively. At the harmonic orders $\nu = 1$ (Figure 5b,f) and $\nu = 3$ (Figure 5d,h) these beams are steered along the *x*-direction, by applying the principle of scattering-pattern shift. Different operations could also be implemented: for instance, Figure S3, Supporting information, illustrates an alternative multi-frequency synthesis implementing two-beam OAM patterns, with possible angular steering.

Another interesting example, which may be relevant for specific applications, involves the possibility to synthesize the same scattering pattern at all harmonic orders. This is illustrated in Figure S4, Supporting Information, for the case of an OAM beam with topological charge $\ell = 1$; in this case, a minimal number $Q = 2$ of sub-sequences is sufficient.

It is worth highlighting that the above examples have not been optimized with specific applications in mind, but rather have been conceived to illustrate the potential of our proposed approach. Clearly, more sophisticated synthesis and accurate tailoring could be obtained by resorting to higher-bit configurations and more complex space–time-coding sequences.

As anticipated, in view of the inherent periodic character of the digital-filter terms in Equation (9), the above syntheses repeat periodically at higher harmonic orders (for both positive and negative values), with progressively decreasing amplitudes governed by the spectral decay in Equation (8). For illustration, Figure S5, Supporting Information, shows the scattering patterns at the harmonic orders $\nu = 4, 5, 6, 7$ pertaining to the example in Figure 3. Qualitatively similar results are observed for the other examples. In some applications, this repetition could be advantageously exploited. For instance, via suitable pattern shaping, this could increase the number of possible

© 2020 Wiley-VCH GmbH

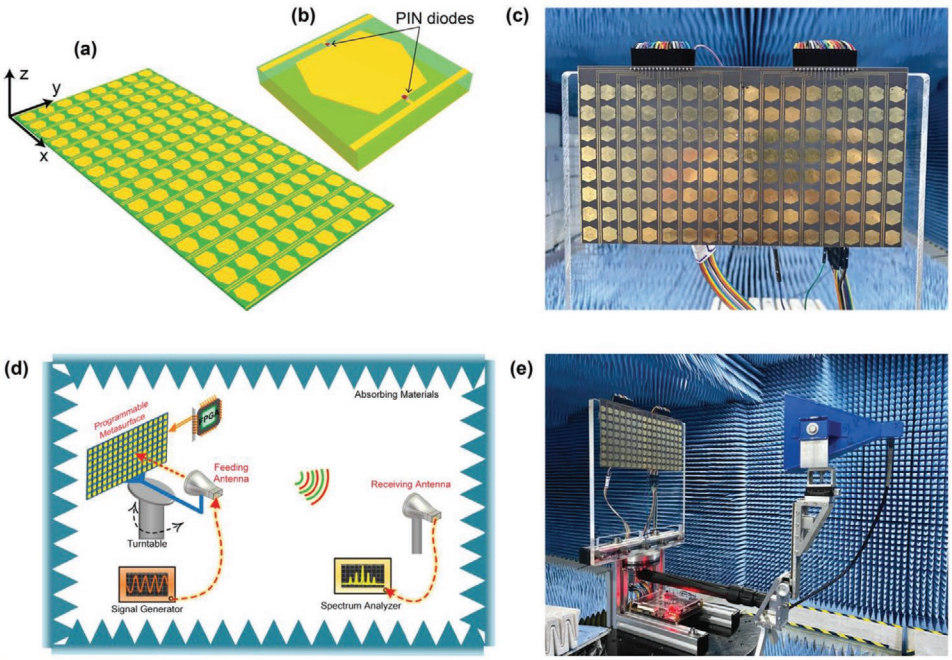

Figure 6. Microwave prototype and experimental setup. a,b) Schematics of the digital metasurface and coding element, respectively. c) Photograph of the fabricated prototype. d,e) Schematic and photograph, respectively, of the experimental setup. In the photograph, the receiving antenna is not shown.

frequency channels, while maintaining sufficient diversity between adjacent frequencies. Moreover, in applications where it is desired to reduce the scattering signature, a broader frequency spreading is actually beneficial to lower the intensity of the scattering peaks. Conversely, in applications where this phenomenon is detrimental, different strategies could be applied in order to mitigate its effects. One possibility is to utilize varactor diodes in the digital metasurface, which would allow smoother modulation waveforms (e.g., sawtooth and sinusoidal), and hence a more rapid spectral decay than the sinc-type in Equation (8). Another interesting alternative, as shown in the Figure S6 (and related discussion), Supporting Information, is the possibility to specifically tailor the temporal coding so as to filter out the higher harmonic orders, thereby increasing the spectral efficiency.

3.2. Experimental Validation

For an experimental proof of concept, as in ref. [26], we rely on a 2-bit space–time-coding digital metasurface featuring of 16×8 coding elements operating at X-band microwave frequencies. Referring to the schematic in **Figure 6**a for illustration, our configuration is organized in 16 columns of eight connected elements sharing common control voltages; this simplifies the electronics at the expense of limiting the beam-shaping/steering capabilities to one plane only (i.e., 1D instead of 2D). The coding element (Figure 6b) is a hexagonal metal patch, printed on a grounded dielectric substrate, connected via two PIN diodes to two biasing lines; the total size of the unit cell is 14×14 mm^2. A photograph of the fabricated prototype (of total size 224×123 mm^2) is shown in Figure 6c. As shown in Figure S7, Supporting Information, for the four possible polarization-state combinations of the two PIN diodes, the structure is numerically designed at the center operational frequency $f_c = 9.5$ GHz so as to provide reflection phases that approximately differ by steps of 90°, with reflection amplitudes always above ≈0.8; these states are accordingly associated to the digits {0,1,2,3}. In practice, we experimentally verified that (apart from an irrelevant common phase), the actual reflection phases are 0°, 101°, 226°, and 268°; these imperfections can be attributed to modeling approximations and inaccuracies (especially in connection with the PIN diodes), parameter uncertainties, and fabrication tolerances.

The experimental setup, schematized in Figure 6d, essentially features an anechoic chamber, a turntable that hosts the prototype and a feeding antenna (connected to a signal generator), and a receiving antenna (connected to a spectrum analyzer); a photograph is shown in Figure 6e.

We apply our joint synthesis at $Q = 4$ harmonic frequencies (i.e., $\nu = 0, 1, 2, 3$), by assuming sub-sequences of length $P = 4$. Accordingly, each of the 16 columns (of eight connected elements) is controlled with a temporal coding of length $L = PQ = 16$, with period $T_0 = 3.2$ µs (i.e., modulation frequency $f_0 = 0.3125$ MHz, corresponding to a diode switching rate of 5 MHz); the corresponding space–time-coding matrix is provided in the Supporting Information. As anticipated, this simplified structure enables a 1D beam shaping/steering (along the θ direction).

Figure 7a–d show (red curves) the numerically computed scattering patterns at the four frequencies of interest, by assuming ideal (90°-step) phase responses for the coding elements. As can be observed, the synthesized patterns are quite distinct, and include: a steered single beam ($\nu = 0$, Figure 7a), a steered difference-beam ($\nu = 1$, Figure 7b), a symmetric dual beam ($\nu = 2$, Figure 7c), and a symmetric dual difference-beam

© 2020 Wiley-VCH GmbH

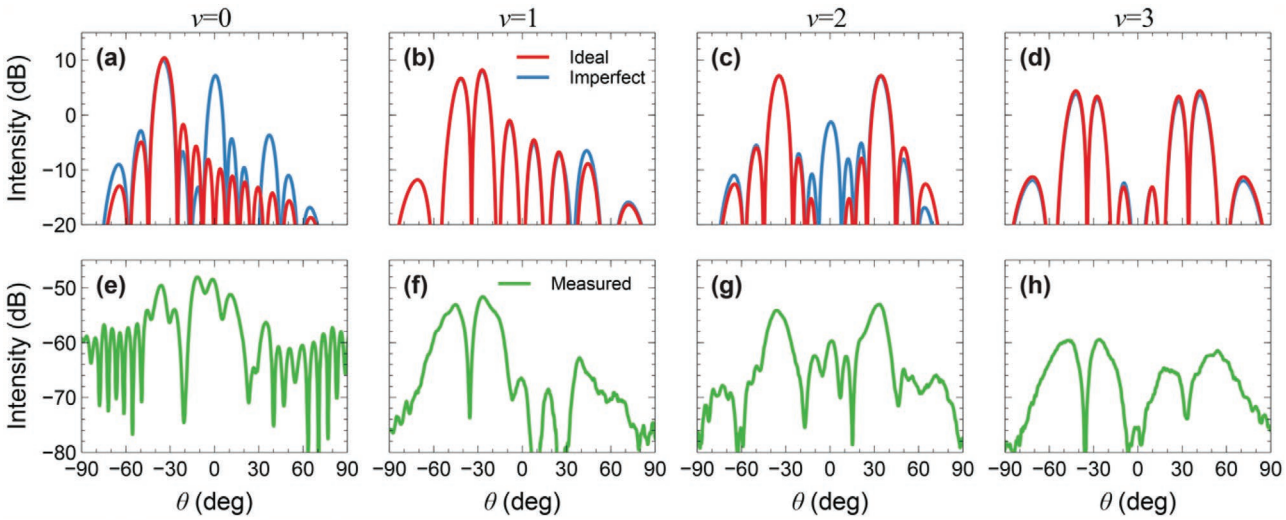

Figure 7. Experimental validation of joint syntheses at $Q = 4$ frequencies, for a 16 × 8-element metasurface with inter-element spacing $d = 0.44\lambda_c$, 2-bit coding ($S = 4$), and sub-sequences of length $P = 4$. a–d) Numerically computed scattering patterns at harmonic orders $\nu = 0, 1, 2, 3$, respectively. Red and blue curves pertain to ideal (90°-step) and imperfect phase responses, respectively. e–h) Corresponding measured results at harmonic frequencies 9.5, 9.5003125, 9.500625, 9.5009375 GHz, respectively. The designed space–time-coding matrix is given in the Supporting Information.

(ν = 3, Figure 7d). Also shown (blue curves), as a reference, are the patterns computed by assuming the aforementioned imperfect phase distributions for the coding elements. The main visible effects of these imperfections are the appearance of additional beams around broadside ($\theta = 0$) for the harmonic orders $\nu = 0$ and $\nu = 2$, whereas the harmonic orders $\nu = 1$ and $\nu = 3$ are only mildly affected.

Figure 7e–h show the corresponding measured patterns. The agreement with the numerical simulations is generally good, especially for those accounting for the phase imperfections. Some differences (e.g., slightly wider beams and higher sidelobes in the measured results) are attributable to the various non-idealities and modeling approximations. At the center frequency ($\nu = 0$, Figure 7e), the moderately worse agreement (especially around the broadside direction) is attributable to the blockage effects of the feeding antenna, which are in fact relevant in view of the imperfection-induced additional beam (see the blue curve in Figure 7a). Qualitatively similar results are obtained for the replicas at higher- and negative-order harmonics, as shown in the Figures S8 and S9, Supporting Information, respectively.

Overall, the above results provide a solid experimental validation, and confirm the practical feasibility of our proposed approach.

4. Conclusions

We have put forward the idea of joint multi-frequency beam shaping and steering of scattering patterns, via space–time-coding digital metasurfaces. Specifically, via the judicious design of intertwined sub-sequences in the temporal coding, we have shown that it is possible to attain the independent and simultaneous syntheses of complex scattering patterns at multiple frequencies. We have presented and discussed several illustrative numerical examples, including multi-beam, diffuse, and OAM-type scattering patterns. Moreover, we have experimentally validated our approach, by fabricating and characterizing a 2-bit prototype operating at microwave frequencies, and demonstrating good agreement between theoretical predictions and measurements.

It is worth highlighting that our proposed approach inherits the programmable and reconfigurable character of the underlying platform, and therefore it is possible to change the synthesized scattering patterns or to spectrally reallocate them "on demand", by simply varying the space–time coding stored in FPGA. This enables a variety of smart functionalities, including self-adaptive and cognitive responses,[59–61] which may find interesting applications within the overarching framework of intelligent reflective surfaces in future mobile-communication,[44–50] imaging,[62,63] and other information systems.[64]

Accordingly, our research agenda includes the development of improved strategies to tailor and control the harmonic power distribution for improved spectral efficiency, including amplitude-phase modulation schemes, as well as the exploration of faster switching mechanisms (e.g., graphene- or VO_2-based) for applications to higher frequencies. Another interesting extension is the joint multi-frequency control of the polarization, which can be pursued by exploiting anisotropic coding elements.[65,66]

5. Experimental Section

Modeling: The approximate modeling in Equations (3)–(5) was implemented numerically via a Python code; for the element scattering pattern, the approximation $E(\theta, \phi) = \cos\theta$ was utilized.

The modeling and design of the 2-bit coding element utilized in the microwave prototype relied on full-wave numerical simulations by means of the commercial software package CST Microwave Studio (see https://www.3ds.com/products-services/simulia/products/cst-studio-suite/). Specifically, for the studies in Figure S7, Supporting Information, a normally incident plane-wave illumination was assumed,

© 2020 Wiley-VCH GmbH

with port-type terminations along the *z*-direction, and periodic boundary conditions in the *x*–*y* plane.

Prototype Fabrication: The prototype in Figure 6c was fabricated via standard printed-circuit-board technology, by using a 1.5 mm thick F4B substrate (relative permittivity = 2.65, loss-tangent = 0.001). Each element was connected to the biasing lines by two PIN diodes (M/A-COM MADP-000907-14020x). The dynamic biasing voltages were provided by an FPGA hardware control board (ALTERA Cyclone IV) preloaded with a computer code that generated the control signals according to the desired space–time-coding matrix.

Measurements: The measurement setup in Figure 6 included a feeding antenna (linearly polarized horn, operating within the 8–12 GHz band) connected to a signal generator (Keysight E8257D) which provided the center-frequency microwave signal. The feeding antenna and the metasurface were coaxially mounted on a rotary support (turntable) at a distance of 0.33 m, and could rotate of 360° in the horizontal plane with 0.1°-step. The harmonic scattering patterns were measured via a receiving antenna (identical to the feeding one) connected to a spectrum analyzer (Keysight E4447A). Measurements were carried out inside an anechoic chamber, and were controlled via a personal computer with General-Purpose-Interface-Bus interface.

The phase responses of the coding elements were measured via a vector network analyzer (Keysight N5230C).

Supporting Information

Supporting Information is available from the Wiley Online Library or from the author.

Acknowledgements

G.C., M.M., and V.G. acknowledge partial support from the FRA Program of the University of Sannio and by the Italian Ministry of Education, University and Research through the PON Program (PM3 project). The work by A.Y.H. had been carried out at the University of Sannio within the framework of the MIT Externship Program, funded by the MIT International Science and Technology Initiatives. L.Z., W.X.T., and T.J.C. acknowledge support from the National Key Research & Development Program of China (2017YFA0700201, 2017YFA0700202, and 2017YFA0700203) and the 111 Project (111-2-05).

Conflict of Interest

The authors declare no conflict of interest.

Keywords

beam shapings, codings, digitals, joint multi-frequency syntheses, metasurfaces

Received: September 6, 2020
Revised: October 14, 2020
Published online:

[1] *Theory and Phenomena of Metamaterials*, (Ed: F. Capolino), CRC Press, Boca Raton, FL **2009**.
[2] W. Cai, V. M. Shalaev, *Optical Metamaterials: Fundamentals and Applications*, Springer, New York **2010**.
[3] C. Caloz, Z. Deck-Léger, *IEEE Trans. Antennas Propag.* **2020**, *68*, 1569.
[4] C. Caloz, Z. Deck-Léger, *IEEE Trans. Antennas Propag.* **2020**, *68*, 1583.
[5] G. Ptitcyn, M. S. Mirmoosa, S. A. Tretyakov, *Phys. Rev. Res.* **2019**, *1*, 023014.
[6] J. R. Zurita-Sánchez, P. Halevi, J. C. Cervantes-González, *Phys. Rev. A* **2009**, *79*, 053821.
[7] J. S. Martínez-Romero, O. M. Becerra-Fuentes, P. Halevi, *Phys. Rev. A* **2016**, *93*, 063813.
[8] J. S. M. Martinez-Romero, P. Halevi, *Phys. Rev. A* **2018**, *98*, 053852.
[9] T. T. Koutserimpas, R. Fleury, *IEEE Trans. Antennas Propag.* **2018**, *66*, 5300.
[10] V. Pacheco-Peña, N. Engheta, *Nanophotonics* **2019**, *9*, 379.
[11] V. Pacheco-Peña, N. Engheta, *Optica* **2020**, *7*, 323.
[12] S. Taravati, G. V. Eleftheriades, *Phys. Rev. Appl.* **2019**, *12*, 024026.
[13] P. A. Huidobro, E. Galiffi, S. Guenneau, R. V. Craster, J. B. Pendry, *Proc. Natl. Acad. Sci. U. S. A.* **2019**, *116*, 24943.
[14] S. Vezzoli, V. Bruno, C. DeVault, T. Roger, V. M. Shalaev, A. Boltasseva, M. Ferrera, M. Clerici, A. Dubietis, D. Faccio, *Phys. Rev. Lett.* **2018**, *120*, 043902.
[15] F. R. Morgenthaler, *IRE Trans. Microwave Theory Tech.* **1958**, *6*, 167.
[16] A. A. Oliner, A. Hessel, *IRE Trans. Microwave Theory Tech.* **1961**, *9*, 337.
[17] R. Fante, *IEEE Trans. Antennas Propag.* **1971**, *19*, 417.
[18] A. Shapere, F. Wilczek, *Phys. Rev. Lett.* **2012**, *109*, 160402.
[19] F. Wilczek, *Phys. Rev. Lett.* **2012**, *109*, 160401.
[20] A. Shaltout, A. V. Kildishev, V. M. Shalaev, *Opt. Mater. Express* **2015**, *5*, 2459.
[21] Y. Hadad, D. L. Sounas, A. Alù, *Phys. Rev. B* **2015**, *92*, 100304.
[22] Y. Hadad, J. C. Soric, A. Alù, *Proc. Natl. Acad. Sci. U. S. A.* **2016**, *113*, 3471.
[23] S. Taravati, N. Chamanara, C. Caloz, *Phys. Rev. B* **2017**, *96*, 165144.
[24] D. Ramaccia, D. L. Sounas, A. Alù, A. Toscano, F. Bilotti, *IEEE Trans. Antennas Propag.* **2020**, *68*, 1607.
[25] J. W. Zang, D. Correas-Serrano, J. T. S. Do, X. Liu, A. Alvarez-Melcon, J. S. Gomez-Diaz, *Phys. Rev. Appl.* **2019**, *11*, 054054.
[26] L. Zhang, X. Q. Chen, R. W. Shao, J. Y. Dai, Q. Cheng, G. Castaldi, V. Galdi, T. J. Cui, *Adv. Mater.* **2019**, *31*, 1904069.
[27] X. Guo, Y. Ding, Y. Duan, X. Ni, *Light: Sci. Appl.* **2019**, *8*, 123.
[28] A. E. Cardin, S. R. Silva, S. R. Vardeny, W. J. Padilla, A. Saxena, A. J. Taylor, W. J. M. Kort-Kamp, H.-T. Chen, D. A. R. Dalvit, A. K. Azad, *Nat. Commun.* **2020**, *11*, 1469.
[29] Z. Wu, A. Grbic, *IEEE Trans. Antennas Propag.* **2020**, *68*, 1599.
[30] T. J. Cui, M. Q. Qi, X. Wan, J. Zhao, Q. Cheng, *Light: Sci. Appl.* **2014**, *3*, e218.
[31] T. J. Cui, S. Liu, L. L. Li, *Light: Sci. Appl.* **2016**, *5*, e16172.
[32] L. Li, T. J. Cui, *Nanophotonics* **2019**, *8*, 703.
[33] L. Zhang, X. Q. Chen, S. Liu, Q. Zhang, J. Zhao, J. Y. Dai, G. D. Bai, X. Wan, Q. Cheng, G. Castaldi, V. Galdi, T. J. Cui, *Nat. Commun.* **2018**, *9*, 4334.
[34] J. Zhao, X. Yang, J. Y. Dai, Q. Cheng, X. Li, N. H. Qi, J. C. Ke, G. D. Bai, S. Liu, S. Jin, A. Alù, T. J. Cui, *Natl. Sci. Rev.* **2019**, *6*, 231.
[35] C. Zhang, J. Yang, L. X. Yang, J. C. Ke, M. Z. Chen, W. K. Cao, M. Chen, Z. H. Wu, J. F. Chen, Q. Cheng, T. J. Cui, *Nanophotonics* **2020**, *9*, 2771.
[36] M. Liu, A. B. Kozyrev, I. V. Shadrivov, *Phys. Rev. Appl.* **2019**, *12*, 054052.
[37] J. Y. Dai, W. Tang, L. X. Yang, X. Li, M. Z. Chen, J. C. Ke, Q. Cheng, S. Jin, T. J. Cui, *IEEE Trans. Antennas Propag.* **2020**, *68*, 1618.
[38] H. Rajabalipanah, A. Abdolali, S. Iqbal, L. Zhang, T. J. Cui, arXiv:2002.06773, **2020**.
[39] S. Fallah, K. Rouhi, A. Abdolali, *J. Phys. D: Appl. Phys.* **2020**, *53*, 085102.
[40] H. Rajabalipanah, A. Abdolali, K. Rouhi, *IEEE J. Emerging Sel. Top. Circuits Syst.* **2020**, *10*, 75.
[41] J. Shabanpour, S. Beyraghi, A. Cheldavi, *Sci. Rep.* **2020**, *10*, 8950.

© 2020 Wiley-VCH GmbH

[42] J. Li, Y. Zhang, J. Li, J. Li, Y. Yang, J. Huang, C. Ma, Z. Ma, Z. Zhang, L. Liang, J. Yao, *Opt. Commun.* **2020**, *458*, 124744.
[43] L. Wang, Y. Zhang, X. Guo, T. Chen, H. Liang, X. Hao, X. Hou, W. Kou, Y. Zhao, T. Zhou, S. Liang, Z. Yang, *Nanomaterials* **2019**, *9*, 965.
[44] E. Basar, M. Di Renzo, J. De Rosny, M. Debbah, M. Alouini, R. Zhang, *IEEE Access* **2019**, *7*, 116753.
[45] C. Huang, A. Zappone, G. C. Alexandropoulos, M. Debbah, C. Yuen, *IEEE Trans. Wireless Commun.* **2019**, *18*, 4157.
[46] Q. Wu, R. Zhang, *IEEE Trans. Wireless Commun.* **2019**, *18*, 5394.
[47] W. Tang, M. Z. Chen, J. Y. Dai, Y. Zeng, X. Zhao, S. Jin, Q. Cheng, T. J. Cui, *IEEE Wireless Commun.* **2020**, *27*, 180.
[48] Q. Wu, R. Zhang, *IEEE Commun. Mag.* **2020**, *58*, 106.
[49] W. Tang, J. Y. Dai, M. Z. Chen, K.-K. Wong, X. Li, X. Zhao, S. Jin, Q. Cheng, T. J. Cui, *IEEE J. Sel. Areas Commun.* **2020**, *38*, 2683.
[50] M. D. Renzo, A. Zappone, M. Debbah, M. Alouini, C. Yuen, J. D. Rosny, S. Tretyakov, *IEEE J. Sel. Areas Commun.* **2020**, *38*, 2450.
[51] L.-H. Gao, Q. Cheng, J. Yang, S.-J. Ma, J. Zhao, S. Liu, H.-B. Chen, Q. He, W. X. Jiang, H. F. Ma, Q.-Y. Wen, L.-J. Liang, B.-B. Jin, W.-W. Liu, L. Zhou, J.-Q. Yao, P.-H. Wu, T. J. Cui, *Light: Sci. Appl.* **2015**, *4*, e324.
[52] S. Liu, T. J. Cui, L. Zhang, Q. Xu, Q. Wang, X. Wan, J. Q. Gu, W. X. Tang, M. Q. Qi, J. G. Han, W. L. Zhang, X. Y. Zhou, Q. Cheng, *Adv. Sci.* **2016**, *3*, 1600156.
[53] M. Moccia, S. Liu, R. Y. Wu, G. Castaldi, A. Andreone, T. J. Cui, V. Galdi, *Adv. Opt. Mater.* **2017**, *5*, 1700455.
[54] M. Moccia, C. Koral, G. P. Papari, S. Liu, L. Zhang, R. Y. Wu, G. Castaldi, T. J. Cui, V. Galdi, A. Andreone, *Sci. Rep.* **2018**, *8*, 11908.
[55] Q. Zhang, C. Liu, X. Wan, L. Zhang, S. Liu, Y. Yang, T. J. Cui, *Adv. Theory Simul.* **2018**, *334*, 1800132.
[56] J. T. Barreiro, T.-C. Wei, P. G. Kwiat, *Nat. Phys.* **2008**, *4*, 282.
[57] F. Tamburini, E. Mari, A. Sponselli, B. Thidé, A. Bianchini, F. Romanato, *New J. Phys.* **2012**, *14*, 033001.
[58] M. Tamagnone, C. Craeye, J. Perruisseau-Carrier, *New J. Phys.* **2012**, *14*, 118001.
[59] T. J. Cui, *Natl. Sci. Rev.* **2018**, *5*, 134.
[60] Q. Ma, G. D. Bai, H. B. Jing, C. Yang, L. Li, T. J. Cui, *Light: Sci. Appl.* **2019**, *8*, 98.
[61] L. Li, Y. Shuang, Q. Ma, H. Li, H. Zhao, M. Wei, C. Liu, C. Hao, C.-W. Qiu, T. J. Cui, *Light: Sci. Appl.* **2019**, *8*, 97.
[62] L. Li, T. J. Cui, W. Ji, S. Liu, J. Ding, X. Wan, Y. B. Li, M. Jiang, C.-W. Qiu, S. Zhang, *Nat. Commun.* **2017**, *8*, 197.
[63] L. Li, H. Ruan, C. Liu, Y. Li, Y. Shuang, A. Alù, C.-W. Qiu, T. J. Cui, *Nat. Commun.* **2019**, *10*, 1082.
[64] T. J. Cui, L. Li, S. Liu, Q. Ma, L. Zhang, X. Wan, W. X. Jiang, Q. Cheng, *iScience* **2020**, *23*, 101403.
[65] Q. Ma, Q. R. Hong, X. X. Gao, H. B. Jing, C. Liu, G. D. Bai, Q. Cheng, T. J. Cui, *Nanophotonics* **2020**, *9*, 3271.
[66] X. G. Zhang, Q. Yu, W. X. Jiang, Y. L. Sun, L. Bai, Q. Wang, C.-W. Qiu, T. J. Cui, *Adv. Sci.* **2020**, *7*, 1903382.

© 2020 Wiley-VCH GmbH